Journal of Materials Chemistry A

Accepted Manuscript

ROYAL SOCIETY OF CHEMISTRY

www.rsc.org/materialsA

Journal Name

RSCPublishing

ARTICLE

Stöber-like Method to Synthesize Ultralight, Porous, Stretchable Fe_2O_3/Graphene Aerogels for Excellent Photo-Fenton Reaction and Electrochemical Capacitors

Cite this: DOI: 10.1039/x0xx00000x

Received 00th January 2012,
Accepted 00th January 2012

DOI: 10.1039/x0xx00000x

www.rsc.org/

Bocheng Qiu,[a] Mingyang Xing,[a*] and Jinlong Zhang[a,b*]

We report three-dimensional (3D) graphene-based hybrids of Fe_2O_3 nanocrystals growth in situ on the graphene aerogels (Fe_2O_3/GAs) by a Stöber-like method. Compared with other reported Fe_2O_3/3D-graphene, Fe_2O_3/GAs has outstanding mechanical strength, high elasticity, ultralight mass, excellent electrical conductivity, efficient oil absorption capacity and nanoparticles dispersion. It has a 3D network structure with a high surface area of 316 m^2 g^{-1} and physicochemical stability. 3D-GAs can inhibit the losing of Fe^{2+} and stabilize the conversion of Fe^{3+}/Fe^{2+} in the Photo-Fenton reaction. Compared with Fe_2O_3 and Fe_2O_3/2D-graphene (Fe_2O_3/GR), Fe_2O_3/GAs gives an ultrastable solar-driven Fenton activity in a wide pH range of 3.5~9.0 for the first time. Besides, nanosized Fe_2O_3 strongly and highly dispersed on the GAs make the composite have a great application in electrochemical capacitors. Although the Fe_2O_3/GAs only contains 18.3 wt% Fe_2O_3, it still yields a high and stable capacitance (151.2 F g^{-1}) at a high discharge current density of 10 A g^{-1}, which is better than Fe_2O_3/GR (93.6 F g^{-1}).

1. Introduction

Many research have been done on Fe_2O_3/three-dimensional (3D) graphene hybrid and its application to lithium ion battery.[1-7] However, there is less report on the application of Fe_2O_3/3D-graphene to the Photo-Fenton reaction and electrochemical capacitors (ECs), up to now. That because most of reported Fe_2O_3/3D-graphene have a large size of Fe_2O_3 and poor particle dispersion on 3D-graphene, which inhibits its application to ECs and Photo-Fenton reaction. Photo-Fenton reaction is a very useful oxidative technology to non-selectively degrade the organic pollutants, especially to the pollutants cannot be degraded by the biotechnology.[8-11] However, there are also some instant shortages to inhibit its industrial application to the environmental issues. The major problems are focused on: 1) the low efficiency for the H_2O_2 utilization;[12, 13] 2) The pH value range for the application is very narrow, and most of the Fenton reaction is conducting at pH < 3.0;[14-16] 3) it is easy to generate the iron cement ($Fe(OH)_3$), which leads to the catalyst deactivation;[17, 18] 4) the Fe_2O_3 powder or liquid Fenton-reagent easily induces the losing of iron ions and is difficult to achieve the recycle. Although some modifications have been done on overcoming above mentioned difficulties,[19-21] there is no great progress in this area to accelerate its industrialization process in the past several decades.

As an ideal support, 3D-graphene or graphene aerogels (GAs) has a special 3D network structure and excellent conductivity,[22-29] which can provide a protective barrier and an efficient charge transport to avoid the occurrence of side reactions.[30-34] The hybrid of Fe_2O_3/GAs has actual application prospects of the development of functional materials in the Photo-Fenton reaction. Hence, if we can achieve the highly dispersed nanosized Fe_2O_3 in situ growth on the GAs, the prepared Fe_2O_3/GAs will have a potential to overcome the above mentioned problems in Photo-Fenton reaction. Moreover, the 3D-macroporous structure of GAs and the small size and highly dispersion of Fe_2O_3 can offer short diffusion path lengths for adsorbing ions and accelerating electron transfer in ECs, which is also beneficial to its ECs performance.[2, 35, 36]

Here we developed an advanced composite of Fe_2O_3 nanocrystals growth in situ on the GAs surface (Fe_2O_3/GAs) by a modified Stöber-like method, which overcomes all above mentioned difficulties in Photo-Fenton reaction at once for the first time. In addition, it also has a good and ultrastable ECs performance.

2. Experimental

2.1 Materials

All chemicals, including iron (III) acetylacetonate $Fe(acac)_3$, H_2SO_4 (AR), $NaNO_3$ (AR), $KMnO_4$ (AR), H_2O_2 (AR), Concentrated ammonia solution (~ 28 wt%), acetonitrile (AR) and ethanol (AR) were used as received without any further purification. Graphite was purchased from Sigma-Aldrich (St. Louis, MO), and ultrapure water was used for all experiments.

2.2 Synthesis of Graphene Oxide (GO)

Graphite oxide (GO) was synthesized from natural graphite powder using a modified Hummers methods.[37] In detail, 2 g graphite powders and 1 g $NaNO_3$ were mixed with 50 mL concentrated H_2SO_4 in an ice bath under vigorous stirring for 2 h. 6 g $KMnO_4$ was added slowly into the mixture while the temperature was kept from exceeding 5 ^oC, then the temperature of the system was heated to 35 ^oC and maintained for 2 h. Afterwards, 80 mL of water was slowly added and then the mixture was heated to 98 ^oC for 1 h. 280 mL of water and 80 mL of 30% H_2O_2 were added to end the reaction. The suspension was then repeatedly centrifuged and washed with 5% HCl solution to remove residual salts. The wet graphite oxide was freeze-dried at 60 ^oC for 24 h.

2.3 Synthesis of the 3D structured Fe_2O_3/GAs composite

By using the Stöber method,[38] it is possible to achieve excellent control of the particle size, narrow size distribution, smooth spherical morphology of the resulting silica or other particles.[39-41] Thereby, we developed a modified Stöber-like method to achieve the highly-dispersed Fe_2O_3 nanocrystals in situ growth on the graphene (Fig. 1). Acetonitrile was used as the co-solvent to improve the solubility of $Fe(acac)_3$ in the mixed solvent. The brief steps are as follows. Typically, 75 mg GO powders were dispersed a mixed solvent containing 75 mL ethanol and 25 mL acetonitrile in an ultrasound bath for 90 min, and then 0.1 mL of NH_3 was added into the suspension at room temperature. After stirring for 30 min, 10 mL $Fe(acac)_3$/ethanol (0.1 mol L^{-1}) was added slowly into the above solution. The suspension was maintained at 80 ^oC for 2.5 h to form the amorphous Fe_2O_3 nanoparticle on the GO sheet. Then the suspension was centrifuged and washed with ethanol to remove excess $Fe(acac)_3$. The as-prepared two-dimensional Fe_2O_3/GO was re-dispersed in 20 mL of water followed by an ultrasonic treatment, which was then transferred into a 50 mL autoclave, and kept at 180 ^oC for 15 h. The aerogels was treated by freeze-drying to obtain a three-dimensional Fe_2O_3/GAs composite.

Fig. 1 Schematic illustration of the in situ growth pathways of highly dispersed Fe_2O_3 nanoparticles on 3D-GAs.

2.4 Synthesis of the 2D structured Fe_2O_3/GR composite

80 mg $FeCl_3$ $6H_2O$ was dissolved in 20 mL of water, then 75 mL of 1 mg/mL GO suspension was added to the $FeCl_3$ solutions under stirring in an ultrasound bath for 90 min, and then the mixture was heated at 90 ^oC for 5 h. When cooled to room temperature, 100 μL of N_2H_4 was added to the mixture to reduce the GO suspension. Then the mixture was put in a microwave oven and irradiated for 180 s. The resulting suspension was centrifuged and washed with deionized water. Finally, the Fe_2O_3/GR was obtained by drying in a vacuum oven.

2.5 Characterization

X-ray diffraction (XRD) patterns of all samples were collected in the range 10-80° (2θ) using a RigakuD/MAX 2550 diffract meter (Cu K radiation, λ =1.5406 Å), operated at 40 kV and 100 mA. The morphologies were characterized by transmission electron microscopy (TEM, JEM2000EX). The surface morphologies were observed by scanning electron microscopy (SEM, JEOL.JSM-6360LV). The instrument employed for XPS studies was a Perkin-Elmer PHI 5000C ESCA system with Al Kα radiation operated at 250 W. The shift of the binding energy due to relative surface charging was corrected using the C1s level at 284.4 eV as an internal standard. Raman measurements were performed at room temperature using a ViaReflex Raman spectrometer with the excitation wavelength of 514 nm. BET surface area measurements were carried out by N_2 adsorption at 77 K using an ASAP2020 instrument. Thermogravimetric and differential thermal analyses were conducted on a Pyris Diamond TG/DTA (PerkinElmer) apparatus at a heating rate of 10 K min^{-1} from 40 to 800 ^oC in air flow. The leaching of Fe^{2+} during reaction was analyzed using a Cary 100 ultraviolet visible spectrometer. In detail, a certain amount of solution was taken from the Photo-Fenton system. Next, a centrifuge separated the supernatant from the solution. And then, 1 mL 1, 10-phenanthroline monohydrate (0.5 wt%) as a testing Fe^{2+} reagent were added into 3mL supernatant. After 15 minutes' standing, the levels of ferrous iron were examined by using a Cary 100 ultraviolet visible spectrometer.

2.6 Photocatalytic Activities

The photocatalytic activity of each catalyst was evaluated by in terms of the degradation of methyl-orange (MO, 10mg/L). The Fe_2O_3/Gas, Fe_2O_3/GR or Fe_2O_3 powder was added into a 100 mL quartz reactor containing 75 mL MO solution. Prior to reaction, the initial pH value of the MO solution was adjusted to 3.5, 5, 7 and 9 with 0.1 M HCl, respectively. Fenton reaction was initiated by adding a known concentration of H_2O_2 (1.2 mL, 30 wt %) to the solution. A 300 W Xe lamp (with AM 1.5 air mass filter) was used as a simulated solar light source. At the given time intervals, the analytical samples were taken from the mixture and immediately centrifuged before filtration through a 0.22 μm millipore filter to remove the photocatalysts. The filtrates were analyzed by recording variations in the absorption in UV-vis spectra of MO using a Cary 100 ultraviolet visible spectrometer.

2.7 Electrochemical measurements

Cyclic voltammetry (CV), galvanostatic charge/discharge experiments and electrochemical impedance spectroscopy (EIS) were performed to evaluate the electrochemical behavior of the samples with a three-electrode cell system in 6 M KOH aqueous electrolyte solution at room temperature. The working electrode was fabricated by pasting a homogeneous slurry of electroactive materials, carbon black and poly(tetrafluoroethylene) in a mass ratio of 80:15:5 into a nickel foam current collector (1×1 cm^2) using a blade, followed by drying at 80 ^{o}C for 12 h and calendaring. A Pt sheet and a Ag/AgCl (KCl-saturated) electrode were used as counter electrode and reference electrode, respectively. The CV galvanostatic charge/discharge and EIS tests were carried out using a CHI 660C electrochemical workstation (Shanghai CH Instrument Company, China). Cycle life test was taken by Land Battery Test System (Wuhan Kingnuo Electronic Company, China). According to the galvanostatic charge/discharge curves, the specific capacitance (Cs, F g^{-1}) can be calculated according to the following equation:

$Cs = I\Delta t / m\Delta V$

where "I (mA)" is charge/discharge current, "Δt (s)" is the discharge time, "m (mg)" represents the mass of electroactive materials in the electrodes, and ΔV (V) is the potential range during discharge.

3. Results and discussion

Compared with the traditional preparation method, we employed a modified Stöber-like technology to make the Fe_2O_3 crystal seeds preliminary growth on the surface of graphene (GR), as shown in Fig. 1 and the HRTEM spectra of Fig. 2. The amorphous and highly dispersed Fe_2O_3 crystal seeds can be clearly observed as indicated by the arrows in Fig. 2b. After a hydrothermal postprocessing, the obtained Fe_2O_3/GAs has an interesting 3D macroscopic appearance (Fig. 3a). Although it contains 18.3 wt% Fe_2O_3 nanocrystals (Fig. S1, in the ESI), its density is still very low (8 mg cm^{-3}) and exhibits an ultralight massive property. Its shape and size can be adjusted by the changing of reaction vessel. With the increasing volume of reaction vessel, the obtained Fe_2O_3/GAs gives an increased size (Fig. 3b). In addition to the interesting macro-appearance, the micro morphology of Fe_2O_3/GAs is also attractive. The SEM of Fe_2O_3/GAs indicates that the Fe_2O_3/GAs has a 3D hierarchical macroporous structure (Fig. 3c-3d). Its surface area can reach to 316 m^2 g^{-1} (Fig. S2a in the ESI), and the pore size distribution curve indicates the presence of hierarchical porous structure (Fig. S2b in the ESI). The mesoporous size is in the range of 10～13 nm, and the macroporous size is in a wide range of 50～120 nm. Granular Fe_2O_3 nanocrystals are one by one embedded in the skeleton of graphene (Fig. 3e). The TEM further confirms the highly dispersed Fe_2O_3 nanocrystals on the surface of graphene (Fig. 3f-3g). The absence of aggregation suggests the Stöber-like process is beneficial to the in situ growth of highly dispersed Fe_2O_3 nanocrystals on the surface of GAs, and the size of Fe_2O_3 is focusing on 25 nm (Fig. 3g, inset). The distribution profile of Fe elements in TEM mapping is consistent with the profile of graphene sheets (Fig. S3 in the ESI), verifying the ultradispersed distribution of Fe_2O_3 nanocrystals on the GAs surface. A high-resolution TEM (HRTEM) image of Fe_2O_3/GAs reveals typical regular lattice fringes with a "d" spacing of 0.25 nm, corresponding to the (110) planes of Fe_2O_3 (Fig. 3h).[42-45] Interestingly, when we take out the Stöber-like process and directly use a hydrothermal treatment to prepare the composite, the results are very different. Though the prepared hybrid also has a GAs appearance, but there are only small amount of Fe_2O_3 loaded on the GAs and some independent nanoparticles fall off from the GAs (TEM images in Fig. S4 in the ESI). Hence, the preliminary growth step is very important to control the Fe_2O_3 size and achieve the in situ and strong growth of Fe_2O_3 on the GAs.

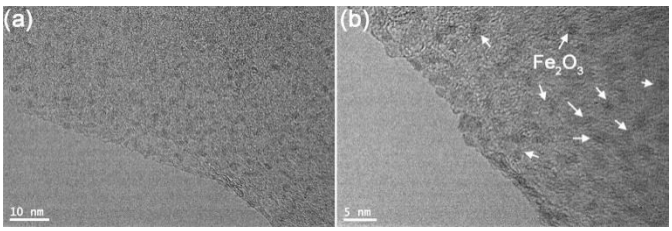

Fig. 2 HRTEM image of the amorphous Fe_2O_3 seeds on the graphene sheet surface during the Stöber-like pretreatment.

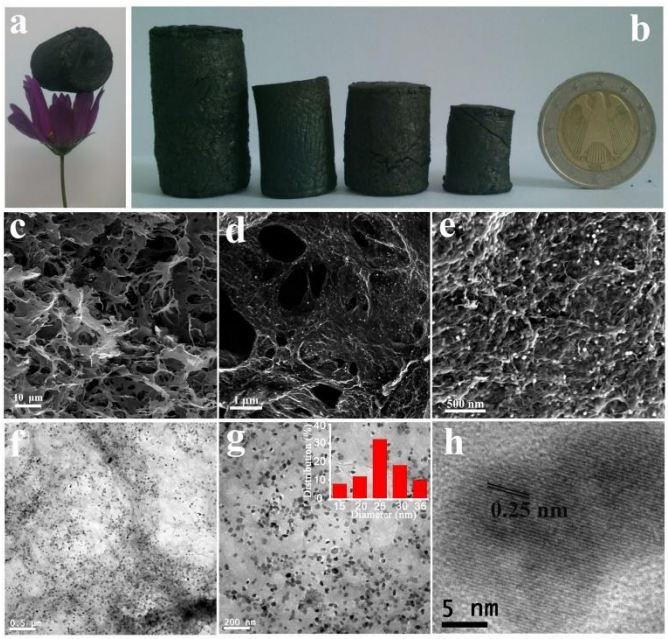

Fig. 3 (a) Photographs of an as-prepared Fe_2O_3/GAs (density of 8 mg cm^{-3}). (b) Photographs of Fe_2O_3/GAs with variable shapes prepared by the changing of reaction vessel (reaction vessel increases from right to left). (c) SEM and (d and e) FE-SEM image of Fe_2O_3/GAs (18.3 wt% Fe_2O_3). (f and g) TEM and (h) HR-TEM images of Fe_2O_3/GAs.

We investigated the structures of the Fe_2O_3/GAs with x-ray diffraction (XRD), Raman spectroscopy, and X-ray photoelectron spectrum (XPS). The strong XRD diffraction peaks of Fe_2O_3/GAs are consistent with the peaks of commercial Fe_2O_3 nanoparticles, indicating that the Fe_2O_3

nanocrystals are highly crystallized (Fig. 4a). The presence of A1g and Eg characteristic peaks in Raman spectra also confirm the generation of highly crystallized Fe_2O_3 in GAs (Fig. 4b). A doublet in the Fe2p XPS region with peaks at 710.8 and 724.4 eV is due to the 2p3/2 and 2p1/2 transition in hematite (Fig. 4c).[42, 46] The solar light responsive Fe_2O_3 nanocrystals in situ growth on GAs are expected to play an important role in the Photo-Fenton reaction. Additionally, the reduction of graphene is also important to the transfer of photo-generated charges in the Fenton reaction and ECs. After hydrothermal treatment, the obvious increase of the intensity ratio of D/G bands in the Raman spectra confirms the reduction of graphene oxide (GO, Fig. 4b).[47-49] The increased reduction degree of Fe_2O_3/GAs ensures the conductivity of graphene. On the other hand, seen from the XPS spectrum of core-level C1s for Fe_2O_3/GAs and GO in Fig. 4d, the reduction of GO during the hydrothermal process is also validated by the decrease of the epoxy C-O-C bonds at 286.7 eV.[1, 50]

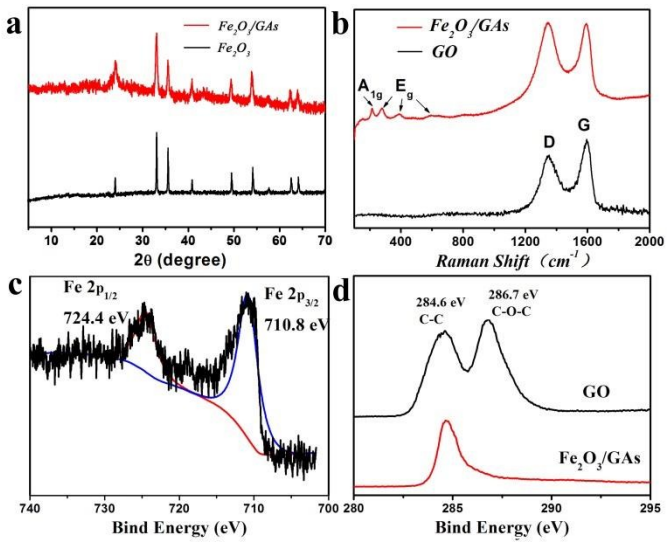

Fig. 4 (a) XRD patterns of Fe_2O_3/GAs and pure Fe_2O_3 powders. (b) Raman spectra of Fe_2O_3/GAs and graphene oxides (GO). (c) Fe2p XPS of Fe_2O_3/GAs. (d) C1s XPS of Fe_2O_3/GAs and GO.

The chemical and physical properties of this advanced composite are also developed in our study, such as the mechanical strength, impedance, oil absorption capacity and excellent thermal stability. The as-prepared Fe_2O_3/GAs can endure dozens of times continuous compression (Fig. 5a). Fe_2O_3/GAs unfolds almost completely after removing the external pressure, indicating it has a fine elasticity and strong mechanical strength (Movie S1). In addition, we have added the stress-strain curve (Fig. S5 in the ESI) to further suggest the excellent mechanical strength of Fe_2O_3/GAs. The stress-strain curve shows plots of compressive stress–strain for the set ε maxima of 30 %, 60 %, and 90 %. The loading process shows two distinct regions, including a linear elastic region ε<70 %, followed by a densification region. In the linear elastic region, the stress increases linearly with the strain. In the densification region ε>70%, the stress rises steeply with compression. Besides, the stress can keep above zero until ε = 0, indicating the high elastic property of Fe_2O_3/GAs. The Fe_2O_3/GAs possesses a macroporous and sandwich biscuit-like structure (Fig. 5b), which is filled with air before being compressed. The impedance of air is much higher than the Fe_2O_3 and graphene, thus, the origin Fe_2O_3/GAs has a large value of impedance, which has excessed the measuring range of ohmmeter (Fig. 5c). When the Fe_2O_3/GAs was compressed by the external force, the sandwich biscuit-like structures are flattened, and the filled air is discharging. Meanwhile, the contact between layer and layer becomes closer and the in-between Fe_2O_3 nanocrystals are also compacted, which are beneficial to the transfer of electrons (Fig. 5b). With the compressing of Fe_2O_3/GAs, its impedance decreases obviously (Fig. 5c). Once removing the external pressure, the structure of Fe_2O_3/GAs unfolds completely, and its impedance also recovers to a large value. The complete impedance testing is shown in the video of Supplementary Movie. S2. The above mentioned controllable impedance of Fe_2O_3/GAs has a large potential application in the electrochemistry devices, such as the electrically controlled switch or probe. In order to highlight the actual value of its controllable impedance, we used the Fe_2O_3/GAs to achieve the adjustment of the speed of the fan (Movie S3). With the compressing of Fe_2O_3/GAs, the fan gave a gradual increased rotating speed.

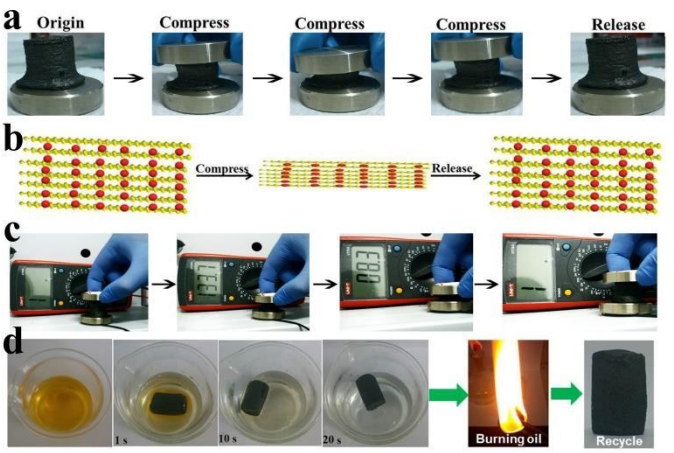

Fig. 5 (**a**) Compression test of Fe_2O_3/GAs. (**b**) Schematic illustration of the structure of Fe_2O_3/GAs during the compression test process. (**c**) The impedance changing of Fe_2O_3/GAs during the compression process. (**d**) Sequential photographs of Fe_2O_3/GAs absorbing pump oil (dyed with Sudan III) on water surface, and the recycle of Fe_2O_3/GAs through the burning of oil.

Some reports have demonstrated that the pure GAs has an excellent oil absorption capacity, owing to its hydrophobicity.[22, 51-55] Although in our study, the Fe_2O_3 nanocrystals were introduced into the GAs 3D-network structure, it still remains the excellent oil absorption (Fig. 5d and Movie. S4). The Fe_2O_3/GAs can completely adsorb the oil in 20 seconds, and it can be recycled by burning off the oil. After the burning, the Fe_2O_3/GAs remains a changeless appearance and can be used again to the oil adsorption (Fig. 5d and Movie. S5). In addition to recycle the Fe_2O_3/GAs, we also can recycle the oil by the distillation method (Fig. S6 in the ESI). After the simple

distillation, the oil can be effective recycling and the yield is more than 95%.

Seen from the above discussion on the chemical and physical characterizations of Fe_2O_3/GAs, it shows a large potential application in the Photo-Fenton reaction. The solar-driven Fenton reaction of the Fe_2O_3/GAs was measured in the presence of H_2O_2, by monitoring the change in optical absorption of a methyl-orange solution (MO, 10 mg/L, Fig. 6a-6c). The commercial Fe_2O_3 and 2D structured Fe_2O_3/GR were used as the reference samples. At the first two times cycling test, the Fe_2O_3 gives a high photodegradation of MO at a low pH value of 3.5 (Fig. 6a). Starting from the third cycling test, its activity exhibits a sharp decrease. When the reaction pH value is higher than 3.0, the Fe^{3+} is very easy to dissolve out and react with the H_2O and OH^- to produce the iron cement of $Fe(OH)_3$, which is covering on the surface of Fe_2O_3 to make the catalyst deactivation. The same tendency is also discovered on the Fe_2O_3/GR. Though the Fe_2O_3/GR has a similar concentration and particle size of Fe_2O_3 with the Fe_2O_3/GAs (TG/DTA and TEM spectra in Fig. S1 and S7 in the ESI, respectively), but its Photo-Fenton reaction activity is much lower than the Fe_2O_3/GAs after the second cycles. The adsorption data of Fe_2O_3/GAs in the dark (blue line in Fig. 6a) can eliminate the affect of adsorption on the Photo-Fenton reaction activity. Although the Fe_2O_3 was also successfully fixed on the 2D-GR (Fig. S7a-S7c, in the ESI), the exposing of Fe_2O_3 in an acidic condition (pH=3.5) would lead to a losing of Fe^{2+} in the solution, thus, resulting into the deactivation of Fe_2O_3/GR in the Photo-Fenton reaction. The TEM spectra of Fe_2O_3/GR after 8 times cycles can verify the dissolving of Fe_2O_3 in the Photo-Fenton reaction (Fig. S7d-S7f, in the ESI). There are less Fe_2O_3 nanoparticles remaining on the 2D-GR surface after 8 cycles. Unlike Fe_2O_3/GR, the 3D-GAs can prevent the Fe^{2+} from dissolving in the solution owing to its 3D-network structure and super-toughness. Hence, even after 10 times cycling test, the degradation rate of Fe_2O_3/GAs remains changeless, which is much higher and more stable than the activity of pure Fe_2O_3 and Fe_2O_3/GR (Fig. 6a). To the traditional Photo-Fenton reaction, the loss of iron ions and the formation of iron cement are all leading to a damage of its micro-morphology. Very interestingly, after 10 times cycling test, the TEM images of Fe_2O_3/GAs indicate the size, the amount and the distribution of Fe_2O_3 nanocrystals on the GAs surface are all changeless (Fig. S8, in the ESI).

In addition to the acidic condition, when the pH value is higher than 7.0, the Fenton reaction activity of Fe_2O_3/GAs is still very high, which is much higher than the pure Fe_2O_3 (Fig. 6b-6c). This advanced composite exhibits an excellent solar-driven Fenton activity in a wide pH range of 3.5～9.0 (Fig. 6b). In order to detect its reaction stability at a high pH value, we carried out the cycling test in a neutral condition (pH = 7.0) which is closer to the actual application (Fig. 6c). To the pure Fe_2O_3, it gives a much lower activity at the first cycle due to the occurring of some side reactions. With the increase of cycling times, the activity of Fe_2O_3 is rapidly inactivated. When the reaction is on the fifth cycle, it almost loses its activity. However, to the Fe_2O_3/GAs, its Fenton activity enhanced significantly. Most importantly, after ten times cycling test, the Fe_2O_3/GAs remains a changeless photo-activity (Fig. 6c).

It is well known that the cycle reaction of Fe^{3+}/Fe^{2+} is very important to the Fenton reaction. The low conversion of Fe^{3+}/Fe^{2+} will decrease the utilization efficiency of H_2O_2 and inhabit the production of hydroxyl free radical. Besides that, the excessed Fe^{3+} ions are easier to generate the $Fe(OH)_3$ in the aqueous solution to make the catalyst inactivation. To the Fe_2O_3 powder, during the solar-driven Fenton reaction process, the Fe^{3+} can capture the photo-generated electrons to form the Fe^{2+} and spread to the MO solution, owing to its better water solubility. Thereby, we can detect a high concentration of Fe^{2+} ions in the aqueous solution (Fig. 6d). These water soluble Fe^{2+} ions can react with H_2O_2 to produce OH• and Fe^{3+} ions. The regenerated Fe^{3+} ions will re-deposit to the surface of Fe_2O_3 to achieve the cycle reaction of Fe^{3+}/Fe^{2+}. However, during the cycle process, the Fe^{3+} ions are easy to react with HO- in an aqueous solution to form the $Fe(OH)_3$ to terminate the cycle reaction of Fe^{3+}/Fe^{2+}, especially when the solution pH value is higher than 3.0. Different from that, the Fe_2O_3/GAs gives a Fe^{3+}/Fe^{2+} cycle reaction on the surface of graphene. Under the solar light irradiation, both dyes and Fe_2O_3 nanocrystals can transfer the photo-generated electrons to the graphene (Fig. 6e), that is, the graphene carries negative charges and attracts positive ions such as Fe^{2+} and Fe^{3+}. The Fe^{3+} ions can capture the photo-generated electrons or react with the H_2O_2 to form the Fe^{2+} ions, which will transfer from Fe_2O_3 to the GAs, owing to the excellent conductivity of graphene. The Fe^{2+} will continue react with H_2O_2 to form the OH• and Fe^{3+} on the surface of graphene. The re-generated Fe^{3+} ions are rapidly reduced to Fe^{2+} by the electrons accumulated on the surface of graphene. The efficiency of Fe^{3+}/Fe^{2+} cycle reaction occurred on the graphene is much higher than the efficiency of reaction occurred in the aqueous solution, owing to the high concentration of electrons on the graphene. The high Fe^{3+}/Fe^{2+} conversion efficiency induces a high concentration of Fe^{2+} on the graphene surface but a low concentration in the aqueous solution (Fig. 6d), further lading to a enhancing generation of OH•. Furthermore, the rapid conversion between Fe^{3+} and Fe^{2+} will significantly reduce the formation of $Fe(OH)_3$, thus, to inhibit the inactivation of catalyst. On the other side, the reduced Fe_2O_3/GAs has a certain of hydrophobicity, which also prevents the generation of $Fe(OH)_3$. Compared with the pure Fe_2O_3 based Fenton reaction, the excellent Fe^{3+}/Fe^{2+} conversion and hydrophobic GAs make the activity and stability of Fe_2O_3/GAs free of the shackles of pH values. Even at a high pH value, the Fe_2O_3/GAs also keeps a high activity and excellent stability (Fig. 6b-6c).

It was worth mentioned that, the Photo-Fenton cycle experiment procedure is very simple (Fig. 7). Put a single Fe_2O_3/GAs in the MO solution, and then irradiation under the 300 W xenon lamp (with an AM 1.5 filter) under a stirring. After a certain time of irradiation, close the light and recycle the Fe_2O_3/GAs by the tweezers. Put the Fe_2O_3/GAs under the solar light irradiation for another 5 minutes to evaporate the

small amount of water and degrade the residual MO molecules on the surface of Fe_2O_3/GAs. After that, the Fe_2O_3/GAs is used for the next cycle experiment.

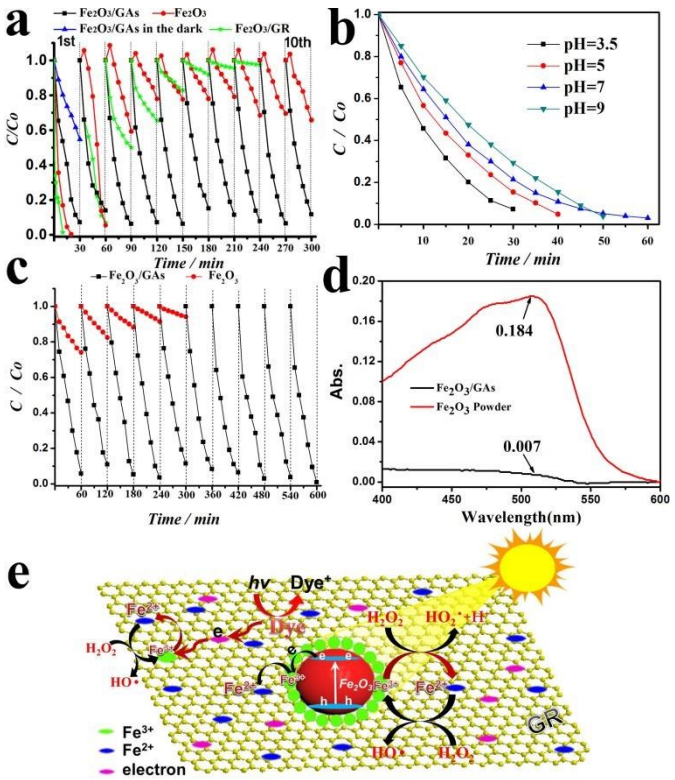

Fig. 6 (**a**) Cycle test for the solar-driven degradation of methyl-orange (75 mL MO, 10 mg/L) under different reaction systems (1.2 mL H_2O_2 (30 wt%), the initial pH was 3.5). (**b**) Solar-driven degradation of MO on Fe_2O_3/GAs (1.2 mL H_2O_2 (30 wt%), the initial pH was adjusted from 3.5 to 9.0 by the adding of 0.1 M HCl). (**c**) Cycle test for the solar-driven degradation of MO on different catalysts with the initial pH of 7.0. (**d**) Absorption spectra of the MO filter liquor photo-degraded by the Fe_2O_3 powders and Fe_2O_3/GAs in the presence of 1, 10-phenanthroline monohydrate (the initial pH was 3.5). (**e**) Photo-Fenton reaction model of Fe_2O_3/GAs in the system containing dye pollutants and H_2O_2.

In order to further demonstrate the Fe^{3+}/Fe^{2+} cycle is occurring on the GAs surface rather than in the aqueous solution, the color changing of the aqueous solution after adding of 1, 10-phenanthroline monohydrate (Phen) is recorded in Fig. S9. The Fe^{2+} ions can react with the Phen to generate the produce with an orange color and a strong visible absorption signal (Fig. 6d and Fig. S9 in the ESI).[56] After adding with Phen, the reaction solution of the Fe_2O_3 powders gives a noticeable orange color, but the reaction solution of the Fe_2O_3/GAs is colorless, indicating the absence of Fe^{2+} ions in the aqueous solution (Fig. S9a, in the ESI). Instead of that, we cut out a small piece of Fe_2O_3/GAs and then smashed it to be the powders, which were dispersed in the reaction liquid to obtain a suspension. After adding the Phen in the suspension, its color changes to orange (Fig. S9b, in the ESI), which indicates the Fe^{2+} ions are mainly located on the GAs surface. Hence, we can conclude that the Fe^{3+}/Fe^{2+} cycle is indeed occurring on the surface of graphene rather than in the aqueous solution, which is the reason why the Fe_2O_3/GAs has an excellent and ultrastable Fenton photocatalytic activity in a wide pH range.

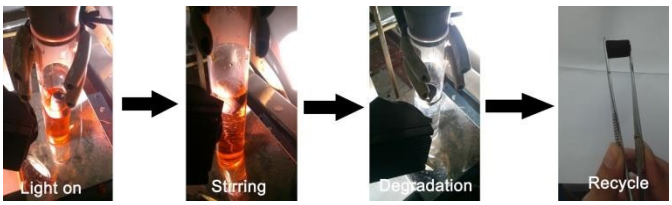

Fig. 7 Photographs of the cycle test of Fe_2O_3/GAs for the solar-driven Photo-Fenton reaction.

In addition to excellent Photo-Fenton reaction activity, the Fe_2O_3/GAs also has an outstanding ECs performance. Cyclic voltammetry (CV) is an ideal tool to indicate the capacitive behavior of materials. Notably, the separation between levelled anodic and cathodic currents of Fe_2O_3/GR at the same scan rates is much smaller than the Fe_2O_3/GAs (CV spectra in Fig. 8a-8b), indicating the advanced capacitance of 3D structured Fe_2O_3/GAs. Compared with Fe_2O_3/GR, the shape of CV curves of Fe_2O_3/GAs is much closer to the rectangle, indicating Fe_2O_3/GAs is a better ECs material. From the galvanostatic (GS) charge/discharge curves of Fe_2O_3/graphene hybrids at different current densities (Fig. S10 in the ESI), we can calculate that the Fe_2O_3/GAs composites present a specific capacitance as high as 151.2 F g^{-1} even at a high discharge current density of 10 A g^{-1}, which is much better than Fe_2O_3/GR (93.6 F g^{-1}). The higher specific capacitance of Fe_2O_3/GAs can be attributed to synergetic effect of higher conductivity of GAs and hierarchical porous structure of Fe_2O_3/GAs. The electrochemical impedance spectroscopy (EIS) for Fe_2O_3/GAs is shown in Fig. 8c. According to analysis of Nyquist plots, the Fe_2O_3/GAs shows a lower charge-transfer resistance and an excellent conductivity, which are convenient to the ion and charge transfer in the electrode materials. The cycling performance of the Fe_2O_3/graphene composites were compared by continuous GS experiments for 1000 cycles at 10 A g^{-1}, as shown in Fig. 8d. Though the Fe_2O_3/GR and Fe_2O_3/GAs are all show high cycling stability even after 1000 cycles, but the specific capacitance retention of Fe_2O_3/GAs is apparently higher than Fe_2O_3/GR. The large surface area and 3D hierarchical porous structure have been considered to be favorable for access of electrolyte solutions.[46] Additionally, the unique and highly dispersed Fe_2O_3 nanocrystals on 3D-GAs provide a narrow distribution in the mesopore range (10~13 nm), which enables electrolyte to access to the electrochemical sites and gives a short diffusion path length for adsorbing ions and accelerating electron transfer. All of above mentioned advantages of Fe_2O_3/GAs determines its long-term electrochemical stability and the outstanding rate capability.

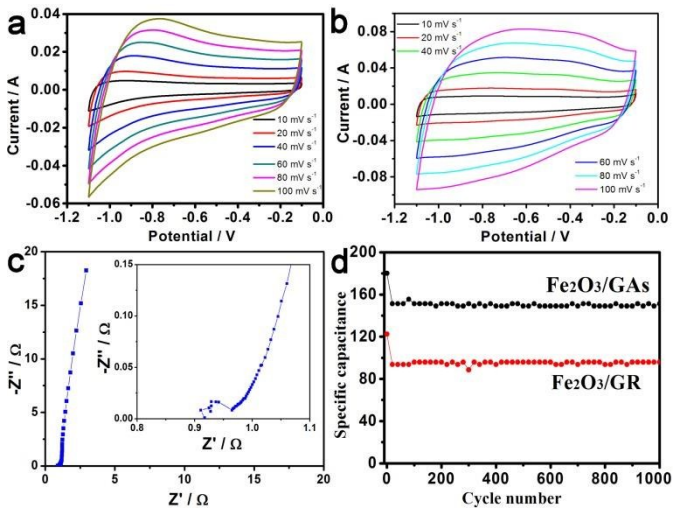

Fig. 8 CV curves of (a) Fe_2O_3/GR and (b) Fe_2O_3/GAs at different scan rates. (c) EIS of Fe_2O_3/GAs (inset is enlarged EIS at low frequency region). (d) Cycling performance of Fe_2O_3/GR and Fe_2O_3/GAs at a current density of 10 A g^{-1}.

4. Conclusions

In conclusion, we developed the ultralight and highly compressible Fe_2O_3/GAs via the Stöber-like pretreatment followed by hydrothermal method. The 3D monolithic Fe_2O_3/GAs exhibits the outstanding performance in Photo-Fenton reaction and ultrastable capacity in ECs application. The outstanding Photo-Fenton activity can be attributed to the excellent conversion efficiency of Fe^{3+}/Fe^{2+} and super-toughness property. Besides, the ultrastable electrochemical capacity can be ascribed to highly dispersion Fe_2O_3, excellent conductivity and 3D hierarchical porous structure. It is believed that our present synthetic route can be further extended to prepare other metal oxides/3D-graphene hybrids as excellent photocatalytic materials, energy storage and conversion devices.

Acknowledgements

This work has been supported by National Nature Science Foundation of China (21237003, 21173077, 21203062, 21377038), National Basic Research Program of China (973 Program, 2013CB632403), the Research Fund for the Doctoral Program of Higher Education (20120074130001) and the Fundamental Research Funds for the Central Universities (22A201514021).

Notes and references

[a] Key Laboratory for Advanced Materials and Institute of Fine Chemicals, East China University of Science and Technology, 130 Meilong Road, Shanghai 200237, P.R. China. E-mail: mingyangxing@ecust.edu.cn; jlzhang@ecust.edu.cn

[b] Department of Chemistry, Tsinghua University, Beijing 100084, P. R. China

Electronic Supplementary Information (ESI) available: [TGA curve, Nitrogen adsorption-desorption isotherms, TEM and elements mapping images, and Galvanostatic charge/discharge curves]. See DOI: 10.1039/b000000x/

1. L. Xiao, D. Wu, S. Han, Y. Huang, S. Li, M. He, F. Zhang and X. Feng, *ACS Appl. Mater. Interfaces*, 2013, **5**, 3764-3769.
2. X. Cao, Z. Yin and H. Zhang, *Energy Environ. Sci.*, 2014, **7**, 1850-1865.
3. Z.-S. Wu, S. Yang, Y. Sun, K. Parvez, X. Feng and K. Müllen, *J. Am. Chem. Soc.*, 2012, **134**, 9082-9085.
4. R. Wang, C. Xu, M. Du, J. Sun, L. Gao, P. Zhang, H. Yao and C. Lin, *Small*, 2014, **10**, 2260-2269.
5. L. Chen, B. Wei, X. Zhang and C. Li, Small, 2013, **9**, 2331-2340.
6. Y. Sun, Q. Wu and G. Shi, *Energy Environ. Sci.*, 2011, **4**, 1113-1132.
7. L. Chen, X. Wang, X. Zhang and H. Zhang, J. Mater. Chem., 2012, **22**, 22090-22096..
8. H. J. H. Fenton, *J. Chem. Soc*, 1894, **65**, 899-910.
9. C. Walling and K. Amarnath, *J. Am. Chem. Soc.*, 1982, **104**, 1185-1189.
10. Z. Miao, S. Tao, Y. Wang, Y. Yu, C. Meng and Y. An, *Microporous Mesoporous Mater.*, 2013, **176**, 178-185.
11. J. Imlay, S. Chin and S. Linn, *Science*, 1988, **240**, 640-642.
12. J. Shi, Z. Ai and L. Zhang, *Water Res.*, 2014, **59**, 145-153.
13. E. Neyens and J. Baeyens, *J. Hazard. Mater.*, 2003, **98**, 33-50.
14. R. G. Zepp, B. C. Faust and J. Hoigne, *Environ. Sci. Technol.*, 1992, **26**, 313-319.
15. C. Walling, *Acc. Chem. Res.*, 1975, **8**, 125-131.
16. C. Ramos Preza, S. Silva Martínez, A. Álvarez Gallegos, J. Vergara Sánchez, C. Pineda Arellano and R. Rodríguez Díaz, *Desalin. Water Treat.*, 2013, **52**, 3526-3534.
17. J. I. Nieto-Juarez and T. Kohn, *Photochem. Photobiol. Sci.*, 2013, **12**, 1596-1605.
18. J. Pignatello, E. Oliveros and A. MacKay, *Crit. Rev. Environ. Sci. Technol.*, 2006, **36**, 1-84.
19. X. Xue, K. Hanna, M. Abdelmoula and N. Deng, *Appl. Catal. B: Environ.*, 2009, **89**, 432-440.
20. R. Andreozzi, V. Caprio and R. Marotta, *Water Res.*, 2002, **36**, 2761-2768.
21. J. H. Ramirez, F. J. Maldonado-Hódar, A. F. Pérez-Cadenas, C. Moreno-Castilla, C. A. Costa and L. M. Madeira, *Appl. Catal. B: Environ.*, 2007, **75**, 312-323.
22. Z.-Y. Wu, C. Li, H.-W. Liang, J.-F. Chen and S.-H. Yu, *Angew. Chem.*, 2013, **125**, 2997-3001.
23. H. Hu, Z. Zhao, W. Wan, Y. Gogotsi and J. Qiu, *Adv. Mater.*, 2013, **25**, 2219-2223.
24. Y. Zhao, C. Hu, Y. Hu, H. Cheng, G. Shi and L. Qu, *Angew. Chem.*, 2012, **124**, 11533-11537.
25. Z. Chen, W. Ren, L. Gao, B. Liu, S. Pei and H.-M. Cheng, *Nat. Mater.*, 2011, **10**, 424-428.
26. H. Sun, Z. Xu and C. Gao, *Adv. Mater.*, 2013, **25**, 2554-2560.
27. X. Huang, B. Sun, D. Su, D. Zhao and G. Wang, *J. Mater. Chem. A*, 2014, **2**, 7973-7979.
28. X. Huang, K. Qian, J. Yang, J. Zhang, L. Li, C. Yu and D. Zhao, *Adv. Mater.*, 2012, **24**, 4419-4423.
29. H.-P. Cong, J.-F. Chen and S.-H. Yu, *Chem. Soc. Rev.*, 2014, **43**, 7295-7325.

30. C. Pei, H. Sun, Z. Zhu, W. Liang, J. An, Q. Zhang and A. Li, *RSC Adv.*, 2014, **4**, 14042-14047.
31. J. Liang, Y. Liu, L. Guo and L. Li, *RSC Adv.*, 2013, **3**, 11489-11492.
32. C. Hu, L. Song, Z. Zhang, N. Chen, Z. Feng and L. Qu, *Energy Environ. Sci.*, 2015, **8**, 31-54.
33. S. Han, J. Jiang, Y. Huang, Y. Tang, J. Cao, D. Wu and X. Feng, *Phys. Chem. Chem. Phys.*, 2015, **17**, 1580-1584.
34. Y. Liu, K. Huang, H. Luo, H. Li, X. Qi and J. Zhong, *RSC Adv.*, 2014, **4**, 17653-17659.
35. C. Liu, F. Li, L.-P. Ma and H.-M. Cheng, *Adv. Mater.*, 2010, **22**, E28-E62.
36. D.-W. Wang, F. Li, M. Liu, G. Q. Lu and H.-M. Cheng, *Angew. Chem. Int. Ed.*, 2008, **47**, 373-376.
37. W. S. Hummers and R. E. Offeman, *J. Am. Chem. Soc.*, 1958, **80**, 1339-1339.
38. W. Stöber, A. Fink and E. Bohn, *J. Colloid Interf. Sci.*, 1968, **26**, 62-69.
39. K. Esumi, T. Hosoya, A. Suzuki and K. Torigoe, *J. Colloid Interf. Sci.*, 2000, **226**, 346-352.
40. R. Vacassy, R. J. Flatt, H. Hofmann, K. S. Choi and R. K. Singh, *J. Colloid Interf. Sci.*, 2000, **227**, 302-315.
41. J. Liu, S. Z. Qiao, H. Liu, J. Chen, A. Orpe, D. Zhao and G. Q. Lu, *Angew. Chem. Int. Ed.*, 2011, **50**, 5947-5951.
42. M. Zhang, B. Qu, D. Lei, Y. Chen, X. Yu, L. Chen, Q. Li, Y. Wang and T. Wang, *J. Mater. Chem.*, 2012, **22**, 3868-3874.
43. H. Wang, Z. Xu, H. Yi, H. Wei, Z. Guo and X. Wang. *Nano Energy* 2014, **7**, 86−96.
44. X. Zhu, Y. Zhu, S. Murali, M. D. Stoller and R. S. Ruoff, *ACS Nano*, 2011, **5**, 3333-3338.
45. J. Zhu, Z. Yin, D. Yang, T. Sun, H. Yu, H. E. Hoster, H. H. Hng, H. Zhang and Q. Yan, *Energy Environ. Sci.*, 2013, **6**, 987-993.
46. S. Yang, X. Song, P. Zhang, J. Sun and L. Gao, *Small*, 2014, **10**, 2270-2279.
47. B. Qiu, M. Xing and J. Zhang, *J. Am. Chem. Soc.*, 2014, **136**, 5852-5855.
48. Y. Huang, D. Wu, S. Han, S. Li, L. Xiao, F. Zhang and X. Feng, *ChemSusChem*, 2013, **6**, 1510-1515.
49. S. Han, J. Wang, S. Li, D. Wu and X. Feng, *J. Mater. Chem. A*, 2014, **2**, 6174-6179.
50. C. Su, M. Acik, K. Takai, J. Lu, S.-j. Hao, Y. Zheng, P. Wu, Q. Bao, T. Enoki, Y. J. Chabal and K. Ping Loh, *Nat. Commun.*, 2012, **3**, 1298-1306.
51. G. Wang, Z. Zeng, X. Wu, T. Ren, J. Han and Q. Xue, *Polym. Chem.*, 2014, **5**, 5942-5948.
52. Z.-Y. Wu, C. Li, H.-W. Liang, Y.-N. Zhang, X. Wang, J.-F. Chen and S.-H. Yu, *Sci. Rep.*, 2014, **4**, 4079-4084.
53. H. Bi, Z. Yin, X. Cao, X. Xie, C. Tan, X. Huang, B. Chen, F. Chen, Q. Yang, X. Bu, X. Lu, L. Sun and H. Zhang, *Adv. Mater.*, 2013, **25**, 5916-5921.
54. B. Kong, J. Tang, Z. Wu, J. Wei, H. Wu, Y. Wang, G. Zheng and D. Zhao, *Angew. Chem. Int. Ed.*, 2014, **53**, 2888-2892.
55. J. Li, J. Li, H. Meng, S. Xie, B. Zhang, L. Li, H. Ma, J. Zhang and M. Yu, *J. Mater. Chem. A*, 2014, **2**, 2934-2941.
56. M. Xing, J. Zhang and F. Chen, *Appl. Catal. B: Environ.*, 2009, **89**, 563-569.

TOC Graphic

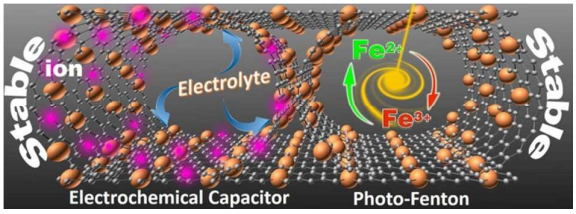

The highly compressible Fe_2O_3/GAs synthesized via the Stöber-like method exhibits the outstanding performance in Photo-Fenton reaction and electrochemical capacitors.